Journal of
Ceramic Science
and Technology

J. Ceram. Sci. Tech., **05** [02] 83-92 (2014)
DOI: 10.4416/JCST2013-00034
available online at: http://www.ceramic-science.com

Numerical Two-Scale Simulations of Damage Evolution at Refractory Materials

D. Henneberg*, A. Ricoeur

University of Kassel, Institute of Mechanics, D-34125 Kassel, Germany;
received October 25, 2013; received in revised form January 6, 2014; accepted February 25, 2014

Abstract

Fracture and damage processes on micro- and mesoscale are combined with macroscale simulations applying numerical multiscale approaches. Cracks and grain boundaries are reproduced in cell models that take account of trans- and intercrystalline crack growth. The global, in general thermomechanical boundary value problem is considered within a continuum mechanics framework. Two approaches are presented combining the scales. Simple processes on the smaller level are described in analytical models including the damage evolution into the constitutive laws by internal variables. More complicated microstructural features are incorporated, performing interacting FE simulations on both scales and applying numerical homogenization schemes.

I. Introduction

In their initial state, damage processes have their origin on the microscopic level. In brittle materials, microcracks develop by means of intergranular decohesion or evolve transgranularly. When a critical volume density of microdamage is reached, a macroscopic crack is formed by coalescence of microscopic defects. Thus, at least two different scales are involved in the damage process. On the larger scale, the whole structure is considered including boundary conditions and macrocrack growth. The smaller scale targets microdefect evolution. A third scale could be involved, looking deeper into the physics of damage including atomic debonding. Owing to multiple interactions, the different levels have to be connected in numerical multiscale simulations.

Different techniques have been developed in this respect starting with pure analytical methods, numerical methods with a strong analytical background and pure numerical approaches. All of them are based on the principle of homogenization, i.e. the smaller scale is reproduced in representative volume elements (RVE) and mapped to the next larger scale introducing effective properties. One problem here is the appropriate choice of boundary conditions for the RVE, supplying a few alternatives, finally leading to different results in terms of effective properties. Among those, Voigt or Reuss approximations should be mentioned, assuming constant strain or stress fields inside the RVE, or periodic displacement boundary conditions yielding results in between the Reuss and Voigt bounds.

Simple defects like idealized straight cracks can be modeled and homogenized analytically. More sophisticated models including e.g. grain boundaries have to be implemented in numerical RVEs, applying e.g. the Finite Element Method (FEM). For linear reversible processes the effective properties, e.g. effective elastic constants, may be determined from RVE simulations being decoupled from the global boundary value problem. In general, those constants will depend on loading multiaxiality, however, not on load history. If damage or other irreversible processes are involved, a fully coupled multiscale FEM-simulation is inevitable.

This work is aimed at the investigation of damage evolution in brittle refractory ceramics under thermomechanical loading. Thus, not only elastic constants have to be coupled in terms of material tangents, but also thermal constants like conductivity or thermal expansion. Owing to the transient features of a thermal shock, the specific heat is also a crucial material property. Assuming a one-way coupling within a single load step, thermal and mechanical boundary value problems can be decoupled.

In a simple model, microcrack growth in a homogeneous matrix is considered analytically and coupled to the thermomechanical FE simulation of the macroscopic problem. A thermal shock sequence is thus simulated. In a more sophisticated model, grain boundaries and intergranular crack growth are considered. First, effective properties are derived from numerical simulations showing the influence of loading multiaxiality on effective stiffness and grain boundary debonding. Second, two-scale coupled FEM-simulations reveal the damage evolution in a polycrystalline brittle solid.

For all numerical simulations, the commercial FE-software ABAQUS is used as solver. It provides interfaces, allowing the implementation of user-defined constitutive laws including damage evolution. Thus, own numerical codes have been developed as Python scripts that finally connect the scales and reproduce the fracture and damage processes. In contrast to classical applications of damage

* Corresponding author: d.henneberg@uni-kassel.de

models, the transient heat conduction problem of a thermal shock has to be coupled with mechanical simulations of damage evolution. Compared to simple analytical assessments, which are still state of the art in the design of refractory devices, the multiscale numerical approach presented in this paper provides a much deeper insight into the physics of thermal shock resistance and enables more sophisticated qualitative and quantitative predictions.

II. Theoretical Framework

(1) Principles of homogenization

In this section, the principle of homogenization will be briefly introduced. It is crucial for macro-meso coupling of numerical simulations. The typical scheme of multiscale methods and homogenization introducing local-scale average properties is illustrated in Fig. 1.

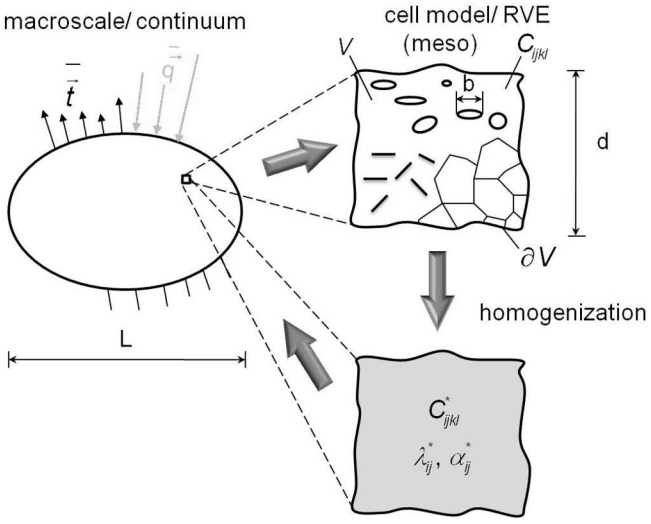

Fig. 1: Thermo-mechanical multi-scale problem and concept of homogenization with effective material properties.

At the macroscale, the refractories are observed as solid continua with thermomechanical initial and boundary conditions given by stresses $\vec{t}$ and heat flux $\vec{q}$ (Neumann) or displacements $\vec{u}$ and temperature θ (Dirichlet). At the micro-level, the geometrical and physical properties of the ceramic microstructure are incorporated by means of a cell model – RVE [1,2], which is generally heterogeneous. The micro- or meso-fields fluctuating along the boundary of the cell model always have to be energetically equivalent to their averages [2]. The macroscopic behavior of refractories depends on heterogeneities. In this paper we consider two different RVE models. One contains a dilute distribution of cracks in an elastic matrix, the other represents cohesive interfaces of grains. The choice of the dimensions of a cell model is a rather delicate task. The extension of the RVE, here denoted by *d*, should be on the one hand much smaller than the characteristic length *L* (the extension of the whole body), on the other much larger than a typical extension of the defect phase b: L > > d > > b. In [3], dimensions from (0.1 mm)³ for metals and ceramics to (100 mm)³ for concrete are suggested. For fine-grained brittle materials, a commonly applied value is $d = 0.1$ mm being related to typical microstructures [4]. The basic equation for an average macroscopic stress field in a simply connected domain *V* is given as

$$\langle\sigma_{ij}\rangle = \frac{1}{V}\int_V \sigma_{ij}(x_i)\,dV = \frac{1}{V}\int_V \sigma_{ik}\delta_{jk}\,dV = \frac{1}{V}\int_V \sigma_{ik}x_{j,k}\,dV \tag{1}$$

where $\delta_{jk} = \vec{e}_j \cdot \vec{e}_k$ is the Kronecker symbol or unit tensor and the stress field σ_j depends on the location x_l. In the case of quasi-static crack growth and without the action of body forces, the momentum balance equals $\sigma_{ik,k}=0$. In this case Eq. (1) can be reformulated according to

$$\langle\sigma_{ij}\rangle = \frac{1}{V}\int_V (x_{j,k}\sigma_{ik} + x_j\sigma_{ik,k})\,dV = \int_V (x_j\sigma_{ik})_{,k}\,dV \tag{2}$$

Applying Gauss's theorem, the average stress $\langle\sigma_{ij}\rangle$ with tractions t_i and the boundary of the RVE δV are obtained:

$$\langle\sigma_{ij}\rangle = \frac{1}{V}\int_{\delta V} x_j\sigma_{ik}n_k\,dA = \frac{1}{V}\int_{\delta V} x_j t_i\,dA \tag{3}$$

The homogenization replaces a heterogeneous material with an equivalent homogeneous material. The scale transition takes place point-wise. Plenty of analytical approaches exist to determine the effective elastic properties for infinitesimal deformations e.g. Reuss [5], Voigt [6], Eshelby [7] or Mori-Tanaka [8]. For a material with complex microstructure, numerical multi-scale methods are necessary. There are many classifications of multi-scale methods, most of them having been developed in recent years. Fig. 2 illustrates an uncoupled numerical homogenization procedure. In the homogenization process, the effective local elastic constants $C^*_{ijkl}(x_l)$ are obtained appearing in a generalized Hook's law which, in case of nonlinear material behavior, represents tangents at the stress-strain curve. Uncoupled homogenization methods for inelastic material behavior are reviewed e.g. in [9,10,11]. The advantage of this method is that the effective material properties need to be determined only once for each load step. For complex nonlinear material behavior, a coupled homogenization approach has to be applied. Fig. 3 depicts a scheme of this method. The effective field variables at each load step and location (integration point) are obtained by averaging the resulting cell model stress field over the RVE. For each integration point at the global macro model (see Fig. 3) the macroscopic strain ε^{macro}_{kl} is obtained. The value of the strain in the macro-level (macroscopic strain) must be equal to the average value of the strain $\langle\varepsilon_{ij}\rangle$ in the meso-level which is obtained by considering the strain averaging theorem for connected RVE domains similar to Eq. (1)

$$\varepsilon^{macro}_{kl} = \frac{1}{V}\int_V \varepsilon^{meso}_{kl}\,dV = \langle\varepsilon_{ij}\rangle \tag{4}$$

with *V* associated to the volume of the RVE. Employing Gauss's theorem, Eq. (4) can be expressed in terms of integrals over the cell model boundary ∂V of an RVE. Similar to Eq. (2), the integral over the surface of the RVE is obtained, i.e.

$$\langle\varepsilon_{ij}\rangle = \frac{1}{2V}\int_{\delta V} (u_i n_j + u_j n_i)\,dA \tag{5}$$

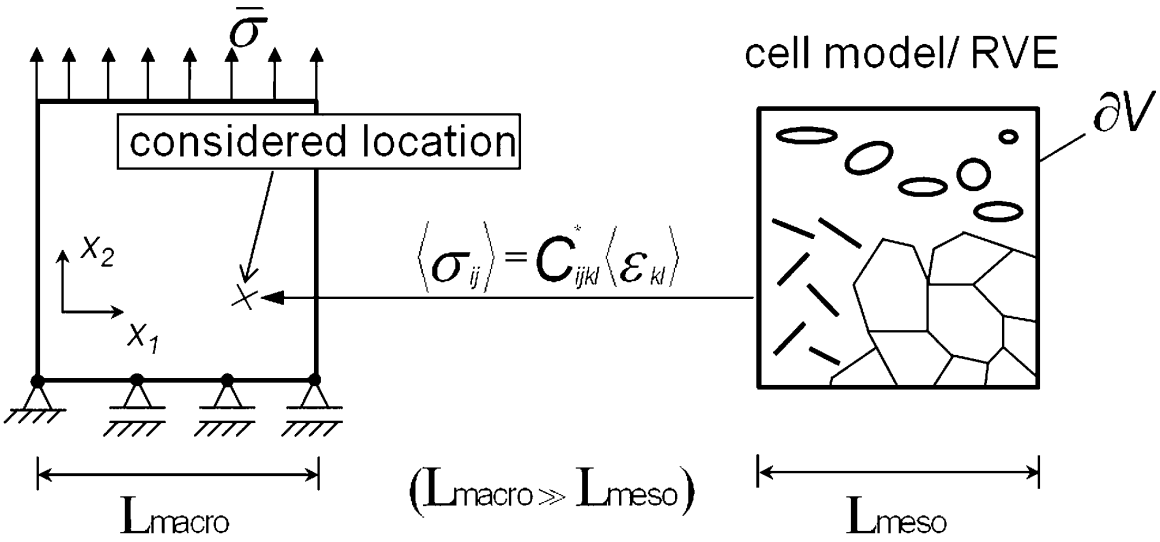

Fig. 2: Scheme of uncoupled homogenization method with point-wise scale separation and effective elastic properties C^*_{ijkl}. Linear relation between macro-strain $\langle \varepsilon_{kl} \rangle$ and macro-stress $\langle \sigma_{ij} \rangle$ in terms of material tangents.

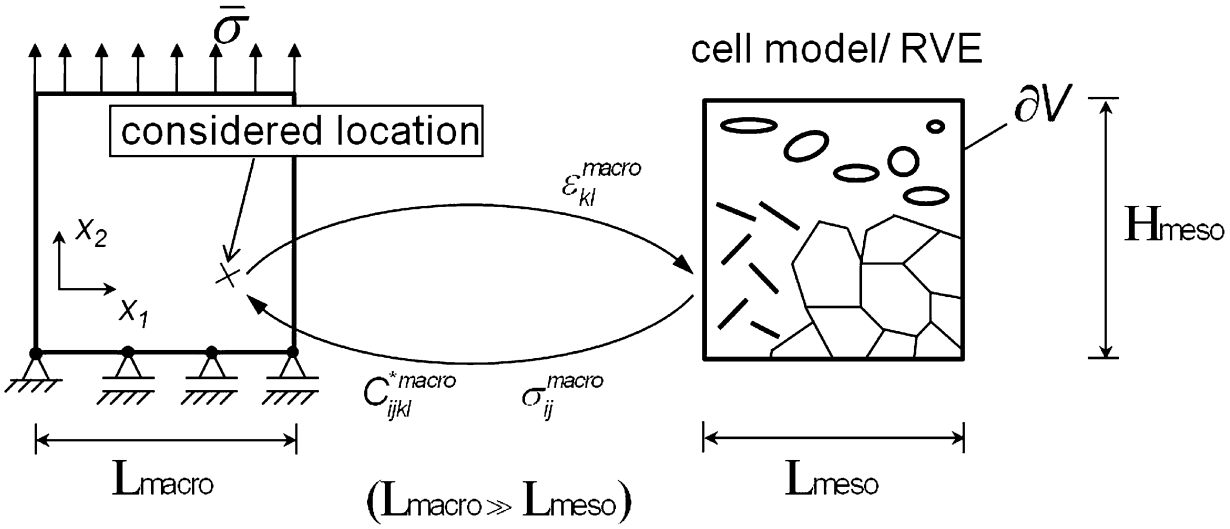

Fig. 3: Coupled homogenization method (meso-macro connection) with point-wise scale separation and macro strain ε^{macro}_{kl} transformed on the RVE boundary to obtain the corresponding macro stress σ^{macro}_{kl} and effective tangent stiffness moduli C^{*macro}_{ijkl}.

The displacements and strains, respectively, are used to formulate the boundary conditions to be imposed on the RVE that is assigned to a specific point. This means, that the macro strain ε^{macro}_{kl} is transformed onto the cell model boundary associated to the relation between strain and displacement as:

$$\left.\begin{array}{c} \varepsilon_{11} x_1 = u_i \\ \varepsilon_{22} x_2 = u_2 \\ 2\varepsilon_{12} = \frac{u_2}{x_1} + \frac{u_1}{x_2} \end{array}\right\} \begin{array}{l} 0 \le x_1 \le L_{meso} \\ 0 \le x_2 \le H_{meso} \end{array} \qquad (6)$$

in which u_i is the displacement within the RVE where $x_1 = L_{meso}$ and $x_2 = H_{meso}$ supply values at the boundaries. Hill-condition postulating the equality of average and local strain energy densities [2] is satisfied by these conditions. After solving the boundary value problem of the cell model, the macroscopic stress tensor σ^{macro}_{ij} and effective tangent moduli C^{*macro}_{ijkl} are obtained. Again, one very important requirement of the scales separation is that the length scale of the global macroscopic model L_{macro} is much larger than the length of the meso scale or cell model L_{meso}. The main ideas of related homogenization methods have been established in [12, 13, 14]. There are similar approaches, e.g. the multi-scale projection method [15] or the FE^2 method [16] typically applied to nonlinear problems with periodic boundary conditions at large deformations. Trends and challenges of the multi-scale homogenization methods are given in [17].

(2) Damage approach based on analytical cell model with microcracks

A simple continuum damage model for thermomechanically loaded brittle refractories based on microcrack initiation and growth has been presented previously in [18]. The material law has been formulated at the macro-level using appropriate homogenization methods, see section II(1), and introducing effective material tensors. Within the framework of continuum damage mechanics, defects e.g. single cracks with initial length *2a* under Mixed-Mode ($\bar{\sigma}_{22}$,$\bar{\sigma}_{12}$) and uniaxial ($\bar{\sigma}_{11}$) loading are introduced into the material law as internal state variables. The average strain

of the microcrack defect phase $(\langle\varepsilon_{ij}\rangle)_C$ embedded in an RVE is defined as [19]

$$\langle\varepsilon_{ij}\rangle_C = \frac{1}{2A}\int_{-a}^{a}(\triangle u_i n_j + \triangle u_j n_i)dx_1 \tag{7}$$

with the displacement jumps $\triangle u_i$ and $\triangle u_j$ of the infinitely thin microcrack, respectively, the area of the RVE A and unit normal vector n_i. The ratio $\frac{4a^2}{A} = f$ will be introduced as damage variable or crack density parameter. Local failure occurs if the damage variable reaches the critical value $f = 1$. The displacement jumps across the crack faces of the defect phase are in the most simple approach taken from a Griffith-crack solution [19], i.e.

$$\triangle u_i(x_1) = \frac{4\langle\sigma_{i2}\rangle}{E}\sqrt{a^2 - x_1^2} \tag{8}$$

with Young's modulus of the matrix material E and the x_1-axis along the crack faces.

The effective inelastic material law for the damaged material in terms of a generalized Hook's law reads:

$$\begin{aligned}\langle\sigma_{ij}\rangle &= C^*_{ijkl}(f)(\langle\varepsilon_{kl}\rangle_C) \text{ or}\\ \langle\varepsilon_{kl}\rangle_M + \langle\varepsilon_{kl}\rangle_C &= (C^*_{ijkl})^{-1}(f)\langle\sigma_{ij}\rangle\end{aligned} \tag{9}$$

Here, C^*_{ijkl} is the fourth-order effective elastic tensor and its inverse $(C^*_{ijkl})^{-1}$ denotes the effective compliance tensor. The average strain of the matrix material is denoted as $\langle\varepsilon_{kl}\rangle_M$. Thus, the stiffness of the microcracked RVE is expressed in terms of an effective elastic tensor including the damage variable f. In order to properly model the thermomechanical coupling, the temperature dependence of material constants is taken into account. The essential thermal parameters of refractory materials influencing reliability and lifetime are thermal conductivity λ_{ij}, thermal expansion α_{ij} and specific heat c_H, where λ_{ij} and α_{ij} are the most important ones. Experiments show that the thermal expansion coefficients and conductivities of refractory materials depend on voids and thermal shock resistant additives [20]. Thermally induced stresses are calculated from Hooke's law introducing the temperature jump $\triangle\theta$

$$\langle\sigma_{ij}\rangle = C^*_{ijkl}\langle\varepsilon^{el}_{kl}\rangle = C^*_{ijkl}(\langle\varepsilon_{kl}\rangle - \alpha^*_{kl}\langle\triangle\theta\rangle) \tag{10}$$

where ε_{kl} is the total strain and ε^{el}_{kl} denotes the elastic strain. Again, quantities with asterisk (*) denote effective material tensors or constants. In order to simulate thermal stress, the temperature distribution in the material is required. Therefore, the transient thermal field problem

$$\rho^* c^*_H \frac{\partial\langle\theta\rangle}{\partial t} = \lambda^*_{ij}\frac{\partial^2\langle\theta\rangle}{\partial x_i \partial x_j} \tag{11}$$

is solved first, supplying a time-dependent temperature field as input data for the mechanical boundary value problem. Owing to the highly dynamic character of thermal shocks, inertia forces are included in the momentum balance:

$$\rho^*\langle\ddot{u}_i\rangle = \langle\sigma_{ij,j}\rangle \tag{12}$$

(3) Cell models with cohesive grain boundaries and intercrystalline crack growth

The special attention of this section is focused on RVEs with multiple grains and cohesive laws on the grain boundaries. Fig. 4 depicts an example of such randomly distributed grains within a volume V with boundary ∂V and outer unit normal n_i.

The dimensions of the RVE are H for the height and L for the length. This cell model (RVE) of a crystal microstructure is used for our simulations. In contrast to the previously presented model of crack distributions in a homogeneous matrix, it establishes the influence of the grain size in our simulations. The RVEs with randomly distributed grains are created automatically based on a parametric preprocessing.

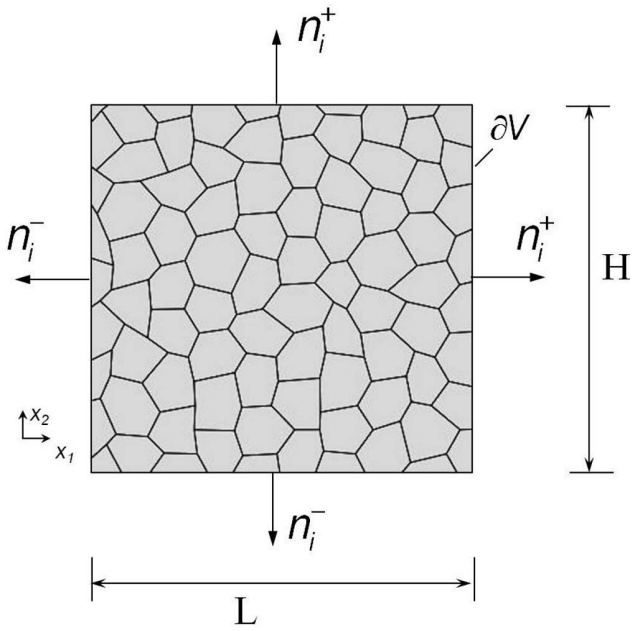

Fig. 4: Representative volume element (cell model) with unit normal vectors n_i representing a polycrystalline material.

In brittle materials, cracks often are initiated and propagate along the interfaces between the crystallites known as grain boundaries (intercrystalline crack growth) [21]. For the sake of simplicity, the separation process is assumed to be based on bi-linear relationships between interfacial traction and separation displacement. Different constitutive laws have been used in cohesive zone models e.g. in Barenblatt's atomic force attraction law [22], in Dugdale's model frequently used for computational fracture research in ductile materials [23], in the cubic model of Needleman [24] or the bi-linear model of Hillerborg [25]. In Fig. 5 the bi-linear cohesive zone law is shown, which is used for the RVE modeling. This traction-separation law allows for computing the relationship between the interface restraining traction σ_R and the relative grain boundary displacement δ, finally leading to an intercrystalline crack if the critical displacement δ^c is attained.

Fig. 6 illustrates a grain boundary interface with all the relevant quantities. Traction vectors t_c and σ_R are related by unit normals as

$$n_c^{+(-)} \cdot \sigma_R = t_c^{+(-)} \tag{13}$$

The bi-linear cohesive law is described by the following equation

$$\sigma_R = \sigma_i^c \begin{cases} (\delta_{(i)}/\delta_{(i)}^0), & 0<\delta_{(i)}<\delta_{(i)}^0 \\ (\delta_{(i)}^0 - \delta_{(i)})/(\delta_{(i)} - \delta_{(i)}^0), & \delta_{(i)}^0<\delta_{(i)}<\delta_{(i)}^0 \end{cases} \quad (14)$$

with index i = n, s for normal and shear separation. To avoid conflicts with the tensorial index notation requiring summation over double indices, brackets have been introduced. In our simulations we use uncoupled cohesive laws, this means, the normal and tangential components of separation are not interacting. For the normal opening mode (Mode I) there are two essential quantities, the peak value of cohesive stress σ_n^c and the related relative interfacial displacement δ_n^0. The condition (σ_n^0/δ_n^0) is the onset of strain softening followed by an instable state, finally leading to crack growth at δ_n^c. In case of shear opening (Mode II), the plot in Fig. 5 is qualitatively identical replacing indices n by s, where σ_s^c denotes the maximum shear stress at δ_s^0. Fig. 7 illustrates schematically a combined normal and shear separation with relative displacements δ_n and δ_s of opposite boundaries of two grains.

From the J-integral enclosing the cohesive zone, the following relation can be derived [26]

$$G_c = \int_0^{\delta^0} \sigma_R(\delta)d\delta \quad (15)$$

The area underneath the entire stress-opening curve (Fig. 5) thus represents the cohesive energy density G_c, i.e. the total energy per unit surface required to completely separate the interface at a given point. It can be interpreted as the fracture energy or in terms of classical linear elastic fracture mechanics the energy release rate.

Integrating the bilinear function according to Eq. (14) and Fig. 5, Eq. (15) yields

$$G_c = \frac{1}{2}\sigma_{(i)}^c \delta_{(i)}^c \quad (16)$$

with index i (i = n, s) for normal and shear sliding traction separation cases. The cohesive law is thus characterized by the cohesive energy. In terms of the crack surface energy, Eq. (16) is converted to

$$2\gamma_c = G_c = \frac{1}{2}\sigma_i^c \delta_i^c \quad (17)$$

where γ_c is the specific fracture surface energy or dissipative energy owing to material separation [27] originally suggested by Griffith [28]. Including the traction vector according to Eq. (13), the cohesive law for both normal and tangential separation can be written down as

$$\begin{Bmatrix} t_n \\ t_s \end{Bmatrix} = \begin{bmatrix} K_{nn} & K_{ns} \\ K_{sn} & K_{ss} \end{bmatrix} \begin{Bmatrix} \delta_n \\ \delta_s \end{Bmatrix} \quad (18)$$

K is the stiffness matrix of the cohesive zone and δ the relative displacement for normal and shear loading. Eq. (18) account for coupling of normal and shear modes, however, in our investigations these is a strict separation choosing $K_{ns} = K_{sn} = 0$. For the cohesive zone modeling between grains, three parameters have to be selected accurately. First, the stiffness matrix K is taken into account, describing the gradients of the straight lines for $\delta < \delta_{(i)}^0$, see Fig. 5. Second, the fracture displacement $\delta_{(i)}^c$ is chosen.

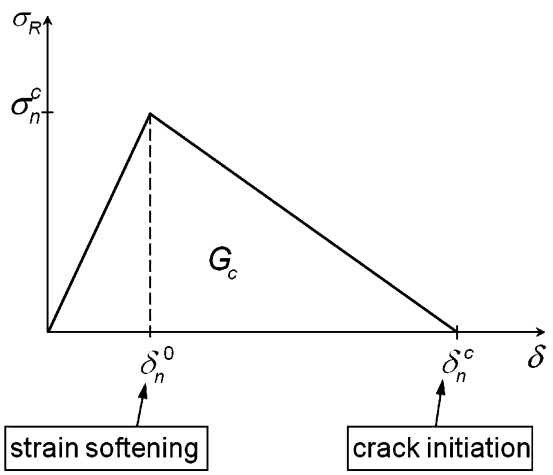

Fig. 5: A bi-linear cohesive zone model relating interface traction σ_R and separation displacement δ [25].

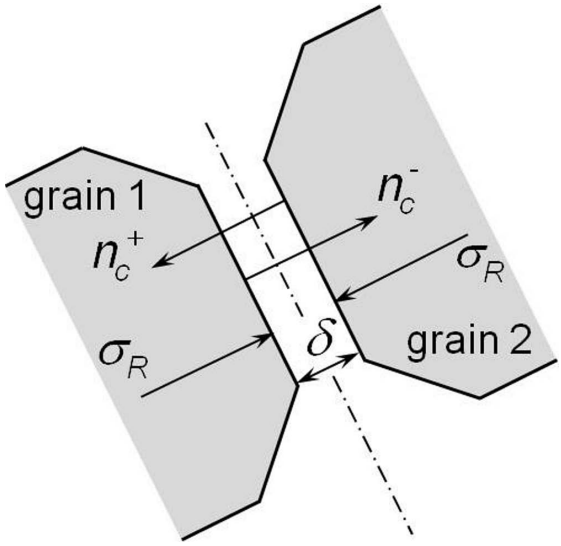

Fig. 6: The cohesive restraining stress σ_R, respective unit normal vectors $n_c^{+(-)}$ and opening displacement δ between two grain boundaries at an interface with pure normal separation.

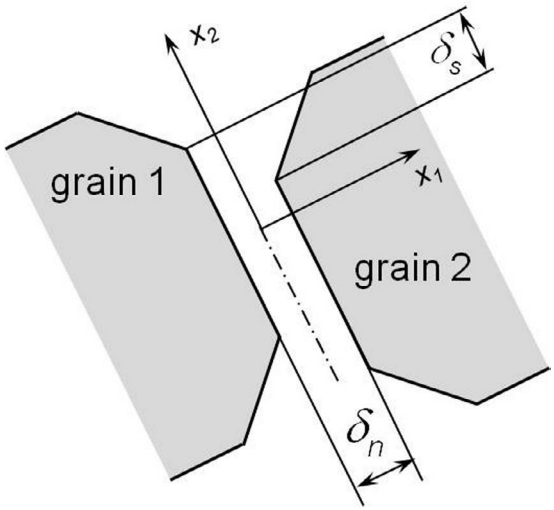

Fig. 7: Separation of opposite surfaces between two grains under Mode I and Mode II loading conditions with normal and shear separation (cohesive zone displacement) and local coordinate system (x_1, x_2).

As third parameter, as mentioned before, the cohesive fracture energy or critical energy release rate G_c needs to be fixed. These parameters determine the effect of intercrystalline crack initiation and growth in an RVE.

III. Numerical Examples

(1) Thermal shock damage with analytical cell model

Cyclic thermal shock tests have been simulated numerically on the basis of application oriented problems and experiments [18,29]. As an example concave, a surface of refractory lining brick was thermally loaded with a local heat flux density of $\dot{q} = 30\ MW/m^2$. The rest of the model boundary is assumed to be adiabatic. Fig. 8 shows the predicted damage pattern in the refractory lining brick after 1, 2 and 3 load cycles, representing states at the ends of the heating periods. The red zones have to be interpreted as macroscopic cracks. The thermal load regime is cyclical, with different durations of constant heat input followed by breaks of 10 s. It is not noteworthy that damage zones are initiated below the surface of the specimen, not approaching its edge before a few load cycles have occurred.

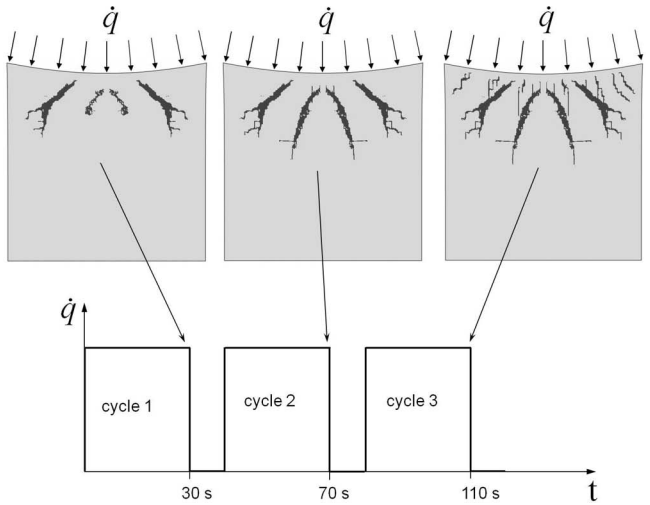

Fig. 8: FE-simulation of cyclic thermal shock tests with a locally absorbed surface heat flux $\dot{q}$ 30 MW/m², 30 s thermal loading + 10 s break. Damage zones are indicated in red.

(2) Effective stiffness constants for polycrystalline model under multiaxial stress state

A cell model (RVE) of a microstructure with randomly distributed grains (see Fig. 4) is considered for the calculation of effective elastic constants under multiaxial stresses in this simulation. Size of the RVE and grains can be selected arbitrarily using a Python script automatically creating the cell model. The grain boundaries are represented by polygons. The mesh predominantly consists of 8-node rectangular elements and is also generated automatically. The bi-linear cohesive law Eq. (14) and the cohesive behavior described in Eq. (18) are implemented along the grain faces to simulate intercrystalline delamination. For the grains isotropic elastic behavior is assumed with Young's modulus E = 105000 MPa and Poisson's ratio $\nu = 0.26$. The elastic constants C_{ijkl} for a singe grain can be defined from these two parameters as

$$C_{ijkl} = \frac{E\vartheta}{(1+\nu)(1-2\nu)}\delta_{ij}\delta_{kl} + \frac{E}{2(1+\nu)}(\delta_{ik}\delta_{jl} + \delta_{il}\delta_{jk}) \quad (19)$$

with the identity or Kronecker tensor δ_{ij}.

Numerical simulations have been performed to investigate crack growth on the meso-scale. Fig. 9 shows the distribution of intercrystalline microcracks under tensile and compressive loading conditions. To demonstrate the principal fracture behavior of polycrystalline materials, the stiffness of the tangential separation K_{ss} has been chosen ten times higher than that of the normal one K_{nn}. Thus, the microcrack initiation and propagation predominantly occurs perpendicular to the maximum principal stresses in the case of tensile loading σ_{22}^0 see Fig. 9a. In the case of compressive loading, see Fig. 9b, cracks can only be driven by shear loading, thus grain boundary separation is predominantly observed at interfaces which are oriented at 45° or less with respect to the loading axis. This behavior is typical for brittle materials under compressive loading [30].

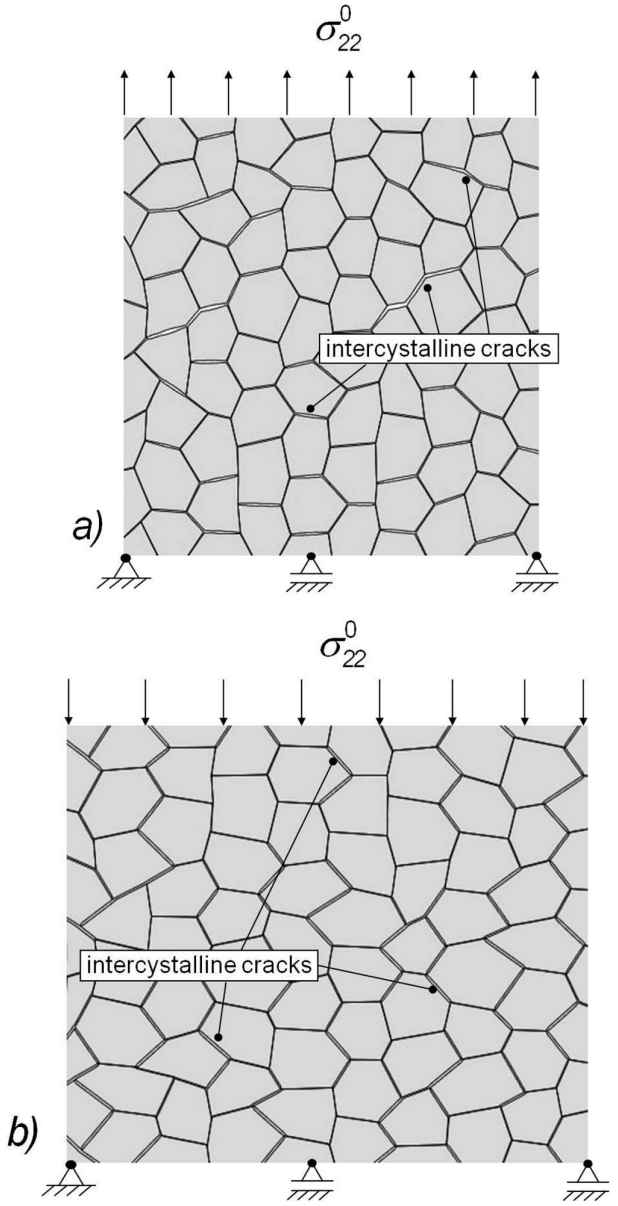

Fig. 9: FE-simulations of intercrystalline microcracks under uniaxial loading conditions: a) tensile loading, b) compressive loading..

Next, effective elastic properties of the polycrystalline material are determined by means of simulations. Here, it is important to choose the size of the cell model properly. An appropriate choice supplies almost isotropic behavior, thus requiring a sufficient number of grains in the RVE. Elastic constants in a classical sense are obtained only if the point of incipient strain softening, i.e. $\delta^0_{(i)}$, is not reached at any interface. Otherwise, the overall constitutive behavior of the RVE is nonlinear and C^*_{ijkl} have to be interpreted as incrementally valid material tangents. In the simulation process, the initial and boundary conditions need to be defined first. The boundary and loading conditions are shown in Fig. 10. A plane stress assumption was used for the simulation. The zoomed region shows the FE mesh. Loading stresses σ^0_{11} and σ^0_{22} are variable quantities enabling the simulation of multiaxial stress states.

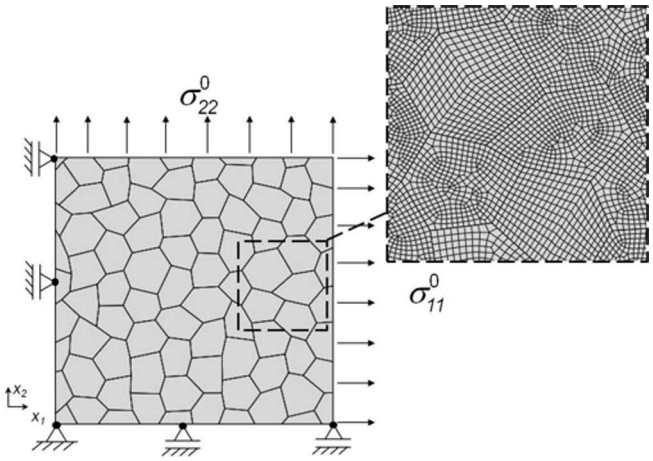

Fig. 10: RVE with arbitrarily distributed grains and boundary/loading conditions in terms of tensile stresses σ^0_{11} and σ^0_{22}, zoomed region shows the FE mesh.

The procedure for the determination of effective elastic quantities is as follows: we hold e.g. tensile loading σ^0_{11} constant and vary tensile loading σ^0_{22}. For each pair of external loads the various deformations ε^0_{ij} and displacements u_i at the boundaries of the cell model are obtained. Based on a Reuss approximation [19] and according to Eq. (4) the average strain $\langle\varepsilon_{ij}\rangle$ for the RVE is determined. As previously mentioned, a suitable choice of the cell model size leads to isotropic conditions, thus the stiffness matrix in compressed Voigt notation is simplified as

$$\begin{bmatrix}\sigma^0_{11}\\ \sigma^0_{22}\\ \sigma^0_{12}\end{bmatrix} = \begin{bmatrix}C^*_{1111} & C^*_{1122} & 0\\ C^*_{1122} & C^*_{1111} & 0\\ 0 & 0 & C^*_{1212}\end{bmatrix}\begin{bmatrix}\langle\varepsilon_{11}\rangle\\ \langle\varepsilon_{22}\rangle\\ \langle\varepsilon_{12}\rangle\end{bmatrix} \qquad (20)$$

Eq. (20) represents an isotropic Hooke's law with the effective stiffness of a material point on the macroscopic scale. Once again it should be borne in mind, that Eq. (20) is valid incrementally for inelastic constitutive behavior. In order to perform the calculation of effective properties, the pseudo-inverse can be used to cope with overdetermined systems of equations.

In Fig. 11, the elastic constant C^*_{1111} is plotted vs. tensile loads σ^0_{11} and σ^0_{22} It is obvious that the values depend on the loading state, particularly on the degree of multiaxiality. In these simulations, the tangential separation K_{ss} has been chosen 1000 times larger than the normal stiffness $K_{nn} = 10^5$ N/mm^3, thus assuming a more or less pure normal separation.

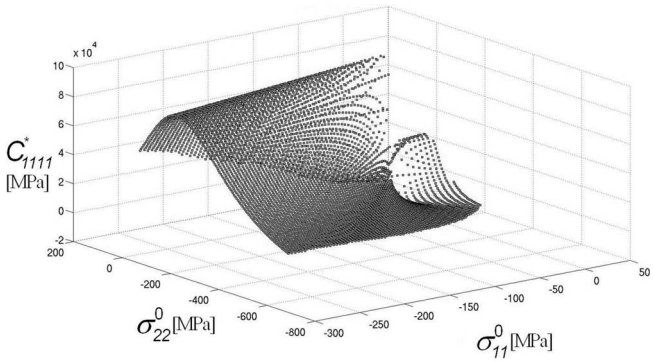

Fig. 11: Effective elastic constant C^*_{1111} vs. biaxial tensile stress ($K_{ss} = K_{nn} \cdot 10^3$).

In Fig. 12, the 3D plot in Fig. 11 has been cut at different values σ^0_{11} The peaks always occur near states of hydrostatic loading. Of course, the plots strongly depend on the parameters K_{nn}/K_{ss}. Since the results in Fig. 11 and Fig. 12 are based on arbitrarily chosen K_{nn}/K_{ss}, the outcomes should be taken as qualitative.

In Fig. 13, the dashed area represents the parameter domain σ^0_{11},σ^0_{22} of linear behavior, i.e. strain softening initiation $\delta^0_{(i)}$ has not occurred at any interface in the RVE. Material points on the macro scale, exhibiting principal stresses within this area, are allocated the respective elastic constants C^*_{ijkl}. Material points with principal stress states outside the dashed domain have to be considered either damaged, if a simple model is taken as a basis, or have to be treated within the framework of a coupled two-scale FE simulation.

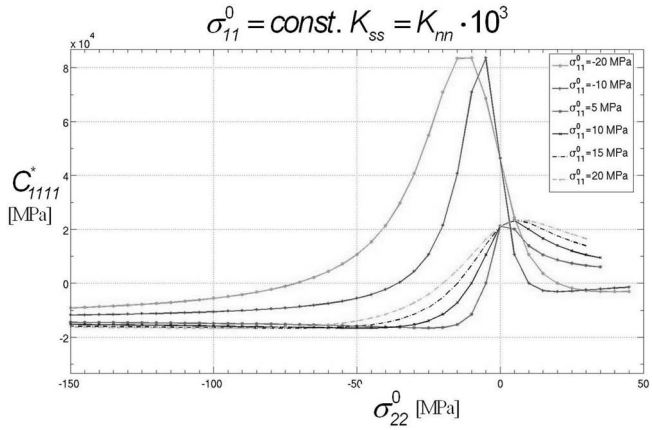

Fig. 12: Effective elastic constant C^*_{1111} vs. σ^0_{22} for different values σ^0_{11}.

(3) Coupled two-scale FE simulation

The meso-macro coupling method as depicted in Fig. 3 can be used to simulate non-linear constitutive behavior and damage evolution. Damage, in general, is related to the energy dissipation and irreversible deformation of the considered brittle material [1, 19]. On a continuum scale, damage is characterized by a mathematical entity describing the ability of momentum transport in a solid body. On

the atomic scale, it can be defined by a net loss of atomic bonds [31]. In our simulations, based on grain separations applying a bi-linear cohesive law according to Eq. (14), failure of an RVE is defined as the state when a few grain boundary nodes attain a cohesive restraining stress of zero, i.e. $\sigma_R = 0$. Thus, the separation displacement at the grain interfaces (compare Figs. 5 and 7) fulfills the condition $\delta_{(i)} \geq \delta^c_{(i)}$. Within this context, the damage variable f is just introduced for the sake of post processing. It is $f = 1$, if the above outlined criterion of rapture is met, otherwise the damage variable remains unchanged, i.e. $f = 0$. At the macro-scale, the material is assumed to be homogeneous, so the properties of the structure are averaged. The external loading is applied at the macro scale. Cell models (meso-level) are solved independently for each integration point. Of course, the two-scale simulation requires an iterative procedure. The solution algorithm for each integration point at the macro-scale is as follows:

1) Initialization of isotropic material properties for macroscopic scale. The damage variable is set to zero. The initiation values of isotropic stiffness C_{ijkl} are calculated from Eq. (19) for the first iteration.
2) The first iteration step at the macro-level is solved.
3) The macroscopic strain field ε^{macro}_{kl} is transformed into equivalent boundary conditions of the cell model in terms of displacements according to Eq. 6).
4) The meso-level iteration step is solved. After convergence, the condition $\delta_{(i)} > \delta^c_{(i)}$ is verified at each grain boundary. If the displacement condition is reached at five nodes, unstable intercrystalline crack growth is implied and the structure is assumed to be locally damaged. The damage variable for the considered integration point is set to one ($f = 1$).
5) If $f = 1$, the local macro-scale stiffness matrix C^{macro}_{ijkl} will be multiplied by 10^{-3}, considerably reducing the stiffness, thus modeling a local rupture. These values will be kept constant at all others iteration steps. In the subsequent iterations, this integration point will no longer be considered.
   If $f = 0$, the average value of the stress on this scale is computed. The average value of stress at the meso-scale $\langle \sigma_{ij} \rangle$ is equal to the value of the stress in the considered point at the macro-scale σ^{macro}_{kl} For the next macro iteration, the stiffness C^{*macro}_{ijkl} (effective tangent stiffness) is determined from Eq. (20) via pseudo inversion.
6) The effective stiffness parameters are passed as solution-dependent state variables to the macro-model for the next load step.

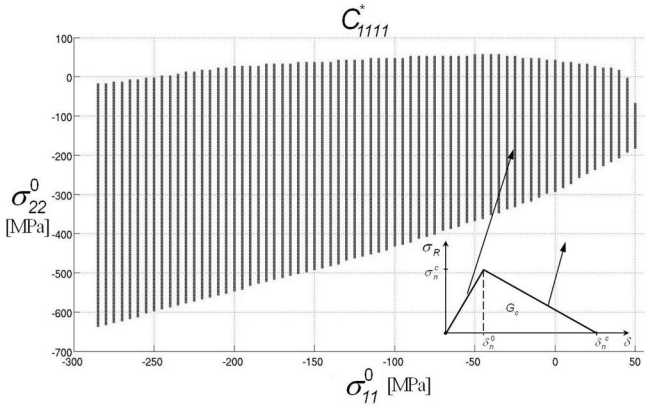

Fig. 13 : Area of linear constitutive behavior in the σ^0_{11} - σ^0_{22}-space.

This simulation process is illustrated in Fig. 14 with the transformed boundary conditions at the RVE edges. In Fig. 15 plates under tensile loading and different damage zones are presented. In a) the tangential stiffness at the grain boundaries is much larger than the normal separation stiffness, in b) it is the other way round. As expected, the damage zones initiate at the notch tip. In the case of large shear stiffness, the zone develops predominantly in the notch plane if the load is increased linearly, whereas a large normal stiffness fosters the formation of two paths under 45°.

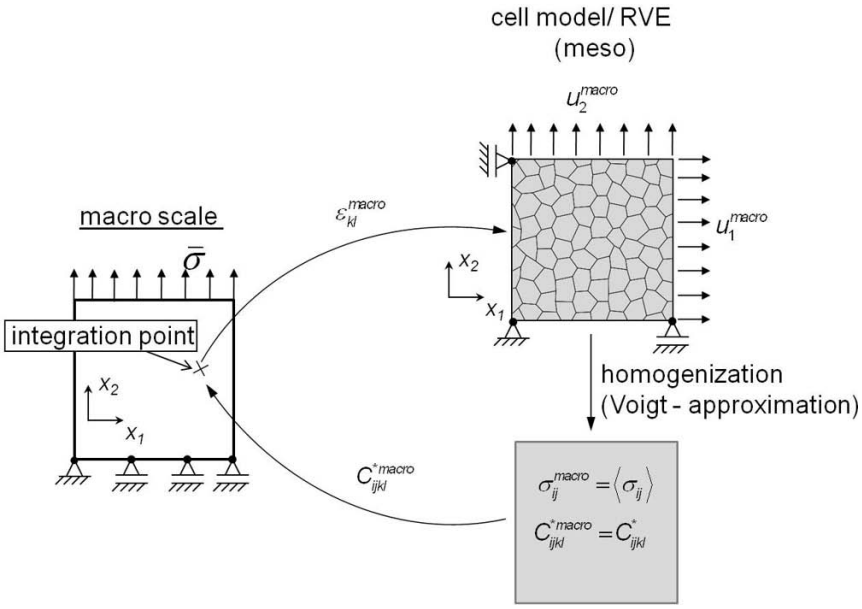

Fig. 14: Principle of macro-meso coupling: plate under tensile loading (macro level) and cell model/RVE with microstructure consisting of grains (meso level).

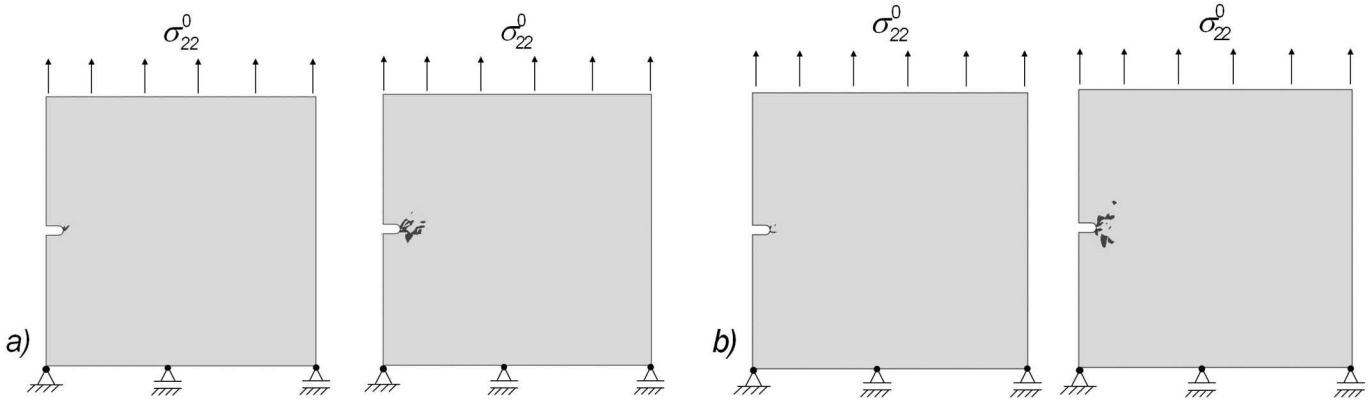

Fig. 15: Notched plate under tensile loading, a) $K_{ss} = K_{nn} \cdot 10^3$, b) $K_{nn} = K_{ss} \cdot 10^3$. Two states of damage evolution.

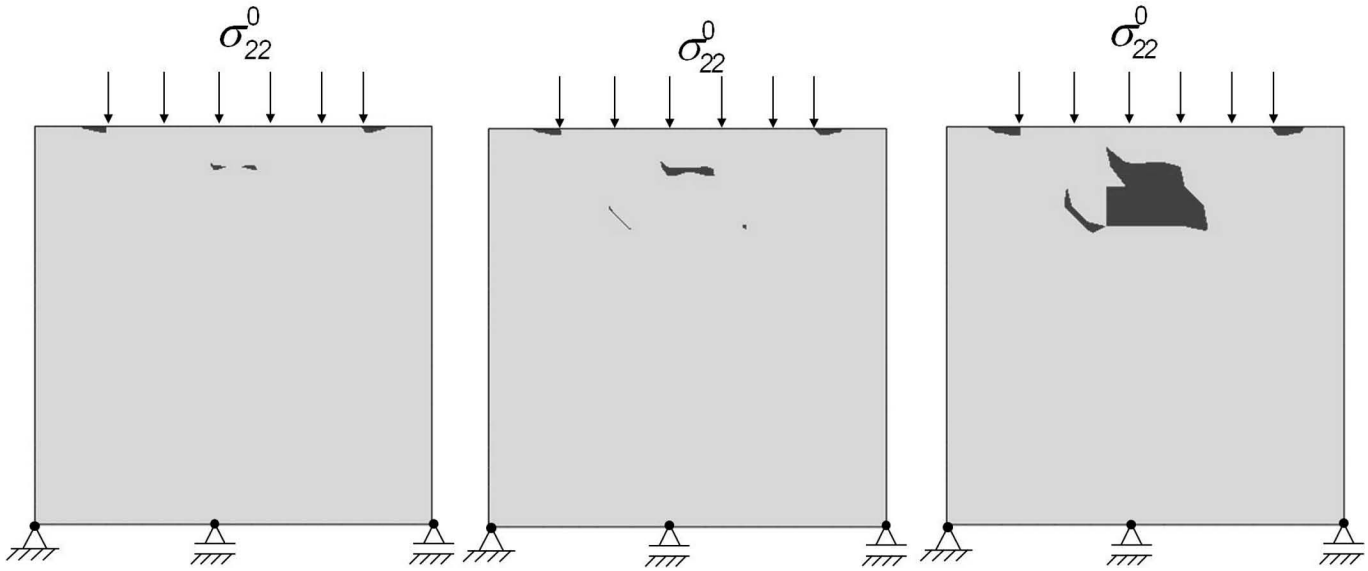

Fig. 16: Plate under compressive loading ($K_{nn} = 100000$, $K_{ss} = 1000000$ N/mm^3) at part of boundary and damage progress.

In Fig. 16 a plate under linearly increasing compressive loading is considered. The load σ_{22}^0 only acts at a part of the upper edge. Damage is initiated both at the singular points at the line load corners and underneath the surface. Damage within the structure increases rapidly if the load is increased.

IV. Conclusions

Damage in brittle materials has been modeled based on two-scale considerations incorporating cracks and imperfect grain boundaries. Both analytical-numerical and pure numerical approaches are presented. Debonding of grain boundaries is described applying cohesive models in connection with bi-linear separation laws. The results provide evidence that promising numerical tools have been developed for the prediction of damage evolution under mechanical and thermomechanical loading. However, some results may still be interpreted just qualitatively. Further research will have to supply more realistic material properties concerning the separation behavior of grain boundaries.

Acknowledgment

Financial support by the German Science Foundation (DFG) within the scope of SPP 1418 is gratefully acknowledged.

References

1 Qin, Q.-H., Yang, Q.-S.: Macro-micro theory on multifield coupling behavior of heterogeneous materials, Springer, Berlin, Heidelberg, New York, 2008.

2 Hill, R.: Elastic properties of reinforced solid, *J. Mech. Phys. Solids*, **11**, 357–372, (1963).

3 Lemaitre, J., Desmorat, R.: Engineering damage mechanics, Springer, Berlin, Heidelberg, New York, 2005.

4 Dormieux, L., Kondo, D., Ulm, F.-J.: Microporomechanics, Wiley, New York, 2006

5 Reuss, A.: Calculating the yield point of mixed crystals bases on the plasticity theory, (in German), ZAMM, **9**, 49–58, (1929).

6 Voigt, W.: The relationship between the two elasticity constants of isotropic bodies, (in German), *Wiedemann Annalen*, **38**, 573–587, (1889).

7 Eshelby, J.D.: The determination of the elastic field of an ellipsoidal inclusion and relation problem, *P. Roy. Soc. Lond. A Mat.*, **241**, 376–396, (1957).

[8] Mori, T., Tanaka, K.: Average stress in matrix and average elastic energy of materials with misfitting inclusions, *Acta Metall. Mater.*, **21**, 571 – 574, (1973).

[9] Zohdi, T., Feucht, M., Gross, D., Wriggers, P.: A description of macroscopic damage through microstructural relaxation, *Int. J. Numer. Meth. Engng.*, **43**, 493 – 506, (1998).

[10] Zohdi, T., Wriggers, P.: Computation micro-macro material testing, *Arch. Comput. Method E.*, **8**, 131 – 228, (2001).

[11] Loehnert, S.: Computation homogenization of microheterogeneous material at finite strains including damage, Diss., Inst. f. Baumechanik und numerische Mechanik, University of Hanover, 2004

[12] Kouznetsova, V.G., Geers, M.G.D., Brekelmans, W.A.M.: Advanced constitutive modeling of heterogeneous materials with gradient-enhanced computational homogenization scheme, *Int. J. Numer. Meth. Engng.*, **54**, 1235 – 1260, (2002).

[13] Gitman, I.M.: Representative volumes and multi-scale modeling of quasi-brittle materials, Ph.D. Thesis, Delft University of Technology, Netherlands, 2006.

[14] Miehe, C., Koch, A.: Computational micro-to-macro transitions of discretized microstructures undergoing small stress, *Arch. Appl. Mech.*, **72**, 300 – 317, (2002).

[15] Loehnert, S., Belytschko, T.: A multiscale projection method for macro/microcrack simulations, *Int. J. Numer. Meth. Engng.*, **71**, 1466 – 1482, (2007).

[16] Oezdemir, I., Brekelmans, M.G.D., Geers, M.: FE^2 computational homogenization for the thermo-mechanical analysis of heterogeneous solids, *Comput. Method Appl. M.*, **198**, 602 – 613, (2008).

[17] Geers, M.G.D., Kouznetsova, V.G., Brekelmans, W.A.M.: Multi-scale computational homogenization: Trends & challenges, *J. Comput. Appl. Math.*, **234**, (7), 2175 – 2182, (2010).

[18] Henneberg, D., Ricoeur, A., Judt, P.: Multiscale modeling for the simulation of damage processes at refractory materials under thermal shock, COMMAT, 70, 187 – 195, (2013).

[19] Gross, D., Seeling, Th.: Fracture mechanics, with an introduction to micromechanics, (in German), Springer, Berlin, Heidelberg, New York, 4th edition, 2007

[20] Aneziris, C.G., Roungos, V.: Usage of nanotechnology in carbon-bonded refractory, Newsletter, Fire, **2**, 4 – 5, (2010)

[21] Wachtman, J.B., Cannon, W.R., Matthewson, M.J.: Mechanical properties of ceramics, 2nd edition. John Wiley & Sons, Inc., New York, 2009

[22] Barenblatt, B.: The formation of equilibrium cracks during brittle fracture, *J. App. Math. and Mech.*, **23**, 622 – 636, (1959).

[23] Dugdale, D.S.: Yielding of steel sheets containing slits, *J. Mech. Phys. Solids*, **8**, 100 – 104, (1960).

[24] Needelman, A.: A continuum model for voids nucleation by inclusion debonding, *J. App. Mech.*, **54**, 525 – 531, (1987).

[25] Hillerborg, A., Modeer, M., Petersson, P.E.: Analysis of crack formation and crack growth in concentrate by means of fracture mechanics and finite elements, *Cement Concrete Res.*, **6**, 773 – 782, (1976).

[26] Rice, J.R.: A path independent integral and the approximate analysis of strain concentration by notches and cracks, *J. Appl. Mech.*, **35**, 379 – 386, (1968).

[27] Kuna, M.: Finite elements in fracture mechanics, Theory-Numerics-Applications, Springer, 2013

[28] Griffith, A.A.: The phenomena of rupture and flow in solids, *Phil. Trans. Roy. Soc.*, 163 – 197, (1920).

[29] Skiera, E., Thomser, C., Linke, J., Roungos, V., Aneziris, C.G.: Thermal shock testing of different carbon bonded MgO-C materials by application of an electron beam test facility, *Refractories Worldforum*, **4**, 125 – 129, (2012).

[30] Ran, X., Zhu, Z., Tang, H.: Experimental study of the failure criterion for brittle materials in compression, *Adv. Mat. Res.*, **320**, 259 – 262, (2011)

[31] Krajcinovic, D.: Selection of damage parameter-art or science?, *Mech. Mater.*, **28**, 165 – 179, (1998).